REFINED LOCAL AND REGIONAL SEISMIC VELOCITY AND ATTENUATION MODELS FROM FINITE-FREQUENCY WAVEFORMS

Zhigang Zhang[2], Yang Shen[2], Li Zhao[3], Po Chen[4], and Xiaoping Yang[1]

Science Applications International Corporation[1] , University of Rhode Island[2], Institute of Earth Sciences, Academia Sinica, Taiwan[3], and Columbia University[4]

Sponsored by Air Force Research Laboratory

Contract No. FA8718-06-C-0014

ABSTRACT

Banana-doughnut sensitivity kernels of travel-time and amplitude variations account for wavefront healing and other diffraction effects that are ignored in the conventional Fermat ray theory. At continental scales one-dimensional (1D) reference models are often adequate and practical to be used in constructing the three-dimensional (3D) kernels. However, at local (e.g., crustal) scales 3D reference models are necessary for further improvement in imaging local and regional velocity structures. Our fully 3D tomography approach addresses this issue and eliminates both the high-frequency (ray) and structural-averaging (1D or 2D reference) approximations.

In previous numerical experiments we have shown the complexity in the sensitivity of finite-frequency head waves to 3D velocity perturbations compared to those predicted by ray theory. The frequency- and distance-dependence of the kernel sampling depth may provide a powerful tool to constrain the vertical velocity gradient in the mantle lithosphere and extend Pn/Sn tomography from presently two dimensions to three dimensions. In the second year of this three-year project we continue to develop and validate the theory and apply the fully 3D finite-frequency sensitivity kernels to synthetic and observed data sets. The systematic tests result in major corrections and ensure the accuracy of the calculation of the kernels. One important finding is that S-velocity anomalies have significant effects on P arrivals. The effects of P-velocity anomalies on S arrivals are much less. This suggests that when waveform-derived travel-time and amplitude anomalies are used in tomographic inversions, P-wave data should be related to not only P velocity but also S velocity. Neglecting this cross-coupling between the waveforms and velocities, as commonly assumed in practice, distorts the forward relation between the model and the data and may cause systematic biases in inversion results. We are carrying out a synthetic tomographic study to explore the power and limitation of the fully 3D finite-frequency kernels.

We are applying this fully 3D method to the eastern Turkey region where there are local and regional broadband waveform records, ground truth (GT) data, and models from previous studies. We use the Program for the Array Seismic Studies of the Continental Lithosphere (PASSCAL) data from the Eastern Turkey Seismic Experiment (ETSE) in 1999-2001. The 29-station network also recorded the Agri Dam explosions. Frequency-dependent travel-time and amplitude anomalies are measured at periods between 3 and 20 s based on narrow-band cross-correlagrams between records and synthetic seismograms calculated by the finite-difference method. These anomalies are used to invert for the perturbations in P- and S-wave speeds using finite-frequency sensitivity kernels. We have also developed the full-wave approach for computing the sensitivity kernels of the travel-time and amplitude anomalies to the perturbations in the Q values. A joint inversion of the same set of frequency-dependent travel-time and amplitude anomalies using the finite-frequency kernels for elastic wave speeds along with those for Q values enables us to account for the effect of both heterogeneity scattering and intrinsic attenuation on the amplitudes of waveforms. We are performing the joint inversions for the regional lithospheric anelastic structure in eastern Turkey and incorporating the calculation of sensitivity kernels for Q values in our fully 3D approach in order to invert for local anelastic structures using the ETSE dataset.

Our objective of this work is to develop refined local and regional velocity and attenuation models for selected areas of interest (AOIs) in Eurasia. We have compiled event and station lists for Korea and the eastern Turkey and northern Iran areas, and continue collecting GT data for model validation.

OBJECTIVES

In this work we obtain Finite-Frequency Seismic Tomography (FFST) velocity models for Eurasia and use them as 3D reference models to refine crustal and shallow upper mantle velocity and attenuation models for focused areas of interest (AOIs) by applying the fully 3D tomography approach.

RESEARCH ACCOMPLISHED

Finite-Frequency Sensitivity Kernels for Head Waves

In the studies of the crust and uppermost mantle, Pn and Sn are often attributed to be the compressional and shear head waves propagating in the uppermost mantle, though strictly a pure head wave is defined in models of uniform plane layers. Because the Pn phase is the first arrival at regional epicentral distances, it has been widely used in detecting and locating seismic events as well as inferring the velocity and attenuation structure of the uppermost mantle. In conventional Pn/Sn travel-time tomography, travel-time variations in Pn or Sn waves are usually attributed to velocity changes right beneath the Moho and in the crust near the source and receiver under ray approximation. Consequently conventional Pn/Sn tomographic inversions solve only the 2D problems of lateral variations in the uppermost mantle and provide no constraints on the vertical structure beneath the Moho. The simplification of horizontal Pn/Sn propagation introduces a bias in the predicted travel times since real waves dive beneath the Moho to depths that depend on the vertical velocity gradient and epicentral distance (Ritzwoller et al., 2002; Hearn et al., 2004). Since tomographic inversions are only as good as the forward problem that describes wave propagation, a practical theory providing a more accurate representation of realistic head waves is needed. The recent development of the finite-frequency seismic theory has made it possible to extract more information from broadband seismograms. Analogues of head waves in a continuous velocity structure, the finite-frequency effects of head waves, which have features distinctly different from turning waves (Aki and Richards, 2002), are yet to be carefully examined.

We obtain the Fréchet kernels of the head waves using the scattering-integral method of Zhao et al. (2005), which applies the principle of reciprocity for the Green's tensors between the points in the 3D model and the receiver. We define the travel-time delay measured by waveform cross correlation between the reference and perturbed waveforms as in Dahlen et al. (2000) and Zhao et al. (2000) and amplitude anomaly as in Zhao et al. (2006). Figure 1a shows the travel time sensitivity kernels for the vertical component Pn for a low velocity layer over half space model. Since the travel-time delay is the volume integration of the product of the kernels and the velocity perturbation, a low-velocity anomaly (negative velocity perturbation) in the negative kernel (red) region, for example, leads to a travel-time delay. Similarly, a low-velocity anomaly in the positive kernel (blue) region results in an earlier arrival. The asymmetry in the kernel is attributed to the difference in the distances from the interface to the source and receiver. At each depth below the source, the intensity of the kernels (the absolute magnitude) is larger on the source side. Right beneath the layer interface and along the ray path, the sensitivity kernels have weak negative values. The kernels become stronger (larger absolute values) horizontally away from the ray path before changing to positive values. A local minimum is clearly visible at the piercing point on the receiver side. All these features are consistent with the results of direct waveform simulation and cross correlation (Zhang et al., 2007). On the vertical profile half way between the source and receiver and perpendicular to the ray path (Figure 1b), the sensitivity decreases with depth from the interface to a minimum (zero) below the ray path. The local minimum is surrounded by strong negative sensitivities in an approximately half circle. The negative-sensitivity half ring is in turn surrounded by bands of positive and negative kernels in approximately half circles, which become narrower and weaker away from the ray path. On the vertical profile containing the source and receiver (Figure 1c), the kernels resemble those of tuning waves in the upper layer but differ significantly in the lower layer. Again the kernels are weak but non-zero along the ray path below the interface. The absolute magnitude of the kernels decreases with depth from the interface to a minimum (zero) before increasing to a maximum, the depth of which increases with the distance to the piercing points on the source or receiver side, whichever is smaller. The downward bending of the sensitivity kernels can be understood as the broadening of the Fresnel zones. The hollow region surrounding the ray path in the upper layer on the receiver side appears to be an upward extension of the local minimum in the lower layer. Unlike the "banana-doughnut" sensitivity kernels for turning waves, the travel-time kernels for the head wave are located on only one side of the ray path below the interface and thus may be characterized as the "split banana-doughnut" sensitivity kernels.

The amplitude sensitivity kernels of the head wave for the same model provide us a different perspective of the head wave behaviors (Figure 2). Comparing the travel-time and amplitude kernels, we note the strong amplitude sensitivity at the location of the local minimum (zero) in the travel-time sensitivity below the interface. We also note that the travel-time and amplitude kernels change their positive or negative values at different depths, thus providing independent and complementary constraints on the velocity structure.

Layer interfaces in the real Earth are rarely exact flat, and the regions that are of geological interest usually have complex layer interfaces as well as vertical velocity variations. Additional numerical studies show that the interface topography has significant effects on the sensitivity kernels (Zhang et al., 2007). The depression or shoaling of the interface compresses or stretches, respectively, the travel-time sensitivity kernels, resulting in increased or decreased sensitivities beneath the interface topography. Because the distribution of the Fréchet kernels is a function of wavelength, head waves are dispersive if the velocity structure in the lower layer has a gradient with depth. Thus the finite-frequency head wave kernels, which account for the possible frequency dependence of the Pn/Sn travel time and amplitude and the deepening of the maximum sensitivity region with the propagation distance due to the broadening of the Fresnel zones, may provide a powerful tool to constrain the vertical velocity gradient in the mantle lithosphere and extend the Pn/Sn tomography from presently two dimensional to three dimensional.

Cross-Coupling of Waveform and Velocity Anomalies

In order to quantitatively assess the numerical accuracy in the calculations of waveforms and further validate finite-frequency kernels, we have carried out a series of numerical tests. We use a uniform medium with a Vp of 6.5 km/s and Vs of 3.5 km/s as the reference model. An explosive or a double-couple source is used to generate synthetic P and/or S waves, which are recorded by a receiver at the same depth (24 km) 53.4 km from the source. The dominant period of the synthetic waveform is 1.2 s. A cylindrically shaped velocity perturbation of 3% Vp or Vs, or both with a height of 6 km and the radius of 3 km is introduced to the reference model in the middle between the source and receiver. The waveforms from the perturbed and unperturbed models are cross-correlated to measure the travel-time and amplitude anomalies caused by the velocity perturbation. The results are compared to the predictions from the finite-frequency kernels. Figure 3 shows the case for the P arrival in a model with an explosive source and both Vp and Vs velocity perturbations. The kernel predictions match the measurements from direct waveform cross-correlation very well in all cases, validating the accuracy of the finite-frequency sensitivity kernels. One important finding of these numerical tests is that the P arrival is affected by both the P- and S-velocity perturbations. The effects of the S-velocity perturbation on the P arrival time and amplitude are roughly 10% of the effects of the P-velocity perturbation of the same magnitude. Since S-velocity anomalies are usually much larger than P-velocity anomalies in the real Earth (e.g., Karato, 1993), the effects of S-velocity perturbations can contribute as much as 20% of the P-wave travel-time and amplitude anomalies. Neglecting this cross-coupling between the waveforms and velocities, as commonly assumed in practice, distorts the forward relation between the model and the data and may cause systematic biases in tomographic inversion results. In contrast, the effects of the P-velocity perturbation on the S arrival are negligible.

Development of Full-Wave Approach to Q Tomography

In our full-wave tomography approach, we quantify the information carried by the recorded waveforms on the 3D structural variations using the so-called frequency-dependent phase and amplitude anomalies. These anomalies are measured from the cross-correlations between the recorded waveforms and the synthetics calculated in a 3D reference model by a fourth-order staggered-grid finite-difference algorithm (Olsen 1994):

$$C(t) = u^0(\mathbf{r}_R, t; \mathbf{r}_S) \otimes u(\mathbf{r}_R, t; \mathbf{r}_S) = \int_{-\infty}^{\infty} u^0(\mathbf{r}_R, \tau; \mathbf{r}_S) u(\mathbf{r}_R, t+\tau; \mathbf{r}_S) d\tau. \tag{1}$$

Here u^0 and u are synthetic and recorded seismograms, respectively, and $\mathbf{r}_S$ and $\mathbf{r}_R$ are locations of the source and the receiver, respectively. The maximum of the cross-correlagram can be used to define the phase delay δT and amplitude increase δA of the recorded seismogram relative to the synthetic:

$$\delta T = -\int_{-\infty}^{\infty} \dot{u}^0(\mathbf{r}_R, t; \mathbf{r}_S) \delta u(\mathbf{r}_R, t; \mathbf{r}_S) dt \Big/ \int_{-\infty}^{\infty} [\dot{u}^0(\mathbf{r}_R, t; \mathbf{r}_S)]^2 dt \,, \tag{2}$$

$$\delta A = \frac{C_M - \tilde{C}_M}{\tilde{C}_M}, \tag{3}$$

where we define the amplitude anomaly in terms of the maximum amplitudes $C_M = C(\delta T)$ of the cross-correlagram and $\tilde{C}_M = \tilde{C}(0)$ of the auto-correlagram of the synthetic seismogram:

$$\widetilde{C}(t) = u^0(\mathbf{r}_R, t; \mathbf{r}_S) \otimes u^0(\mathbf{r}_R, t; \mathbf{r}_S) = \int_{-\infty}^{\infty} u^0(\mathbf{r}_R, \tau; \mathbf{r}_S) u^0(\mathbf{r}_R, t+\tau; \mathbf{r}_S) d\tau. \tag{4}$$

Frequency-dependent measurements are achieved by narrow-band filtering the cross-correlations around a number of discrete frequencies across the frequency range of interest. Upon applying the representation theorem (e.g., Aki and Richards, 2002) and the Born approximation, the waveform perturbation δu can be expressed as (e.g., Zhao et al., 2005)

$$\delta\mathbf{u}(\mathbf{r}_R, t; \mathbf{r}_S) = \int_{\oplus}\int_0^t [\nabla \mathbf{G}^0(\mathbf{r}_R, t-\tau; \mathbf{r})]^{213} : [\delta\rho(\mathbf{r})\mathbf{I}\partial_{\tau\tau} - \delta\mathbf{C}(\mathbf{r})] : [\nabla \mathbf{u}^0(\mathbf{r}, \tau; \mathbf{r}_S)] d\tau\, d^3\mathbf{r}\ , \tag{5}$$

where $\delta\rho(\mathbf{r})$ and $\delta\mathbf{C}(\mathbf{r})$ are the model perturbations in density and the fourth-order elasticity tensor, respectively, $\mathbf{I}$ is the fourth-order identity tensor, and the symbol $[\cdot]^{213}$ indicates the transposition of a third-order tensor between its first and second indices (Ben-Menahem and Singh, 1981), i.e., $[\cdot]^{213}_{ijk} = [\cdot]_{jik}$. For the perturbation of any specific structural parameter such as the *S*-wave speed β, the expression for its phase-delay or amplitude increase Fréchet kernel can be derived by selecting the elements of $\delta\mathbf{C}(\mathbf{r})$ in eq.(5) corresponding to β, substituting the resulting equation for $\delta\mathbf{u}(\mathbf{r}_R; \mathbf{r}_S)$ into eq.(2) or (3), and identifying the kernel for the spatial integral. For example, the Fréchet kernel for the amplitude increase due to the perturbation in shear-wave speed β is

$$K_A^\beta(\mathbf{r}_R; \mathbf{r}; \mathbf{r}_S) = \int_{t_1}^{t_2} 2\rho\beta \mathbf{u}(\mathbf{r}_R, t; \mathbf{r}_S) \cdot \mathbf{K}_u^\beta(\mathbf{r}_R; \mathbf{r}, t; \mathbf{r}_S) dt \Big/ \int_{t_1}^{t_2} |\mathbf{u}(\mathbf{r}_R, t; \mathbf{r}_S)|^2\ dt, \tag{6}$$

where the waveform kernel for shear-wave speed β is

$$\mathbf{K}_u^\beta(\mathbf{r}_R; \mathbf{r}, t; \mathbf{r}_S) = \int_{-\infty}^{\infty} \{[\nabla \mathbf{G}(\mathbf{r}_R, t-\tau; \mathbf{r})]^{213} : [(\nabla\mathbf{u}) + (\nabla\mathbf{u})^{\mathrm{T}}] - 2(\nabla\cdot\mathbf{G}^{\mathrm{T}})[\nabla\cdot\mathbf{u}(\mathbf{r}, \tau; \mathbf{r}_S)]\}\, d\tau. \tag{7}$$

When anelastic attenuation is considered, the bulk and shear moduli in the elasticity tensor $\delta\mathbf{C}(\mathbf{r})$ are analytically extended into frequency-dependent complex-valued quantities with the introduction of quality factors Q_κ and Q_μ :

$$\kappa = \kappa(\omega)[1 + iQ_\kappa^{-1}(\omega)], \quad \mu = \mu(\omega)[1 + iQ_\mu^{-1}(\omega)]. \tag{8}$$

For convenience in seismology, Q_κ and Q_μ can be related to the quality factors for the compressional and shear waves Q_α and Q_β. Perturbing eq.(8)

$$\delta\kappa = \delta\kappa(\omega)[1 + iQ_\kappa^{-1}(\omega)] + i\kappa(\omega)\delta[Q_\kappa^{-1}(\omega)], \quad \delta\mu = \delta\mu(\omega)[1 + iQ_\mu^{-1}(\omega)] + i\mu(\omega)\delta[Q_\mu^{-1}(\omega)]. \tag{9}$$

and substituting the perturbations in the new complex bulk and shear moduli into eq.(5), we can derive the expressions of the Fréchet kernels for Q_α and Q_β in the same way as we derive the expressions for the kernels in eqs.(6) and (7). Assuming that the quality factors are frequency-independent, the

$$K_A^\beta(\mathbf{r}_R; \mathbf{r}; \mathbf{r}_S) = \int_{t_1}^{t_2} 2\rho\beta \mathbf{u}(\mathbf{r}_R, t; \mathbf{r}_S) \cdot \mathbf{K}_u^{Q_\beta}(\mathbf{r}_R; \mathbf{r}, t; \mathbf{r}_S) dt \Big/ \int_{t_1}^{t_2} |\mathbf{u}(\mathbf{r}_R, t; \mathbf{r}_S)|^2\ dt, \tag{10}$$

$$\mathbf{K}_u^{Q_\beta}(\mathbf{r}_R; \mathbf{r}, t; \mathbf{r}_S) = -Q_\beta^{-1} H[\mathbf{K}_u^\beta(\mathbf{r}_R; \mathbf{r}, t; \mathbf{r}_S)], \tag{11}$$

where $H[f(t)]$ denotes the Hilbert transformation of the function $f(t)$. We have implemented the Fréchet kernel calculations for the quality factors using coupled normal-mode summations and are in the process of implementing these calculations using finite-difference method to invert for the anelastic crustal structures in selected AOIs.

We have carried out preliminary tomography inversions for shear-wave speed β and quality factor Q_β for East Asia using regional Rayleigh wave phase and amplitude anomalies (Zhao and Chen, 2006). Our dataset consists of broadband Rayleigh waves that traverse Eastern Eurasia. The seismic records were recorded on instruments from the Incorporated Research Institutions for Seismology (IRIS) global seismographic Network (GSN), cooperating networks such as the Chinese Digital Seismic Network (CDSN), and several IRIS PASSCAL experiments from Asia. All data were collected from IRIS DMC. The stations used are distributed in the region from 10ºN to 60ºN and 80ºE to 140ºE. We used stations recording either an LHZ or BHZ components, with a total of 72 stations. Events occurred in the region between 10ºN to 60ºN and 70ºE to 140ºE in the time period between 2000 and 2006. The magnitudes are greater than Mw 6. The total number of events collected was 151. The initial dataset was cleaned to remove data with a signal-to-noise level of less than approximately 2 in the central portion of the frequency band

(0.02-0.1 Hz), as well as data clearly contaminated by glitches or other problems. The final number of records used is 3160 from 146 events.

Full-Wave Tomography for Eastern Turkey

Northern Iran and eastern Turkey are tectonically active regions with abundant and relatively diffused seismicity. The Eastern Turkey Seismic Experiment, along with several other seismic stations in the area, provides an excellent waveform data set to develop and test the fully 3D tomography approach. We have implemented the full-wave tomography approach to an area in Eastern Turkey using the waveform dataset from the Eastern Turkey Seismic Experiment (ETSE) (Sandvol et al., 2003a,b; Al-Lazki et al., 2003; Gok et al., 2003; Turkelli et al., 2003; Zor et al., 2003). Figure 4 shows the distribution of the 29 ETSE stations and the epicenters of the 124 regional events located by the ETSE records (Turkelli et al., 2003). As a first iteration of our iterative full-wave anelastic tomography, we selected 19 ETSE stations within a study area of roughly 350 km x 300 km (down to 55-km depth) and 24 earthquakes for which the focal mechanisms are available (Turkelli et al., 2003). The study area and the locations of stations and earthquakes are shown in Figure 5.

In our first 3D tomography attempt, we used the layered crustal model MENA 1.1 (Walter et al., 2000) as the reference model. In order to model the wave interactions with the highly variable Moho interface in this region, we modified the bottom part of MENA 1.1 to allow for lateral variations in the Moho depth based on the results from the receiver function study of Zor et al. (2003). In the study area, the Moho depth changes from 38 km in the southern part to 50 km in the north.

We used a fourth-order staggered-grid finite-difference algorithm (Olsen 1994) to compute the synthetic seismograms in the layered crustal model with variable Moho depth. The crustal model has a minimum shear-wave speed of 1.1 km/s. In our finite-difference simulations, we used a grid spacing of 300 km, resulting in reliable waveforms up to a nominal frequency of about 0.5 Hz. Then the frequency-dependent phase and amplitude anomalies between the synthetic and recorded seismograms are measured for the 69 source-receiver paths shown in Figure 5 at 0.1 Hz, 0.15 Hz, 0.2 Hz, 0.25 Hz, 0.3 Hz, 0.35 Hz and 0.4 Hz. Measurements along several source-receiver paths are shown in Figure 6. Note that in our definitions for the phase and amplitude anomalies, positive measurements indicate phase delays and amplitude increases in the records relative to corresponding synthetics.

In order to compute the Fréchet kernels of the measurements with respect to the elastic and anelastic mode parameters, we have also calculated the receiver strain Green tensors (RSGTs) for all 19 stations as well as the source strain Green tensors (SSGTs) for the 24 events; see Zhao et al. (2006) for details of the Fréchet kernels using the RSGTs and SSGTs. The numerical calculations were carried out using 32 processors on a Linux cluster. The calculations took about two weeks of wall-clock time. The resulting SGT database occupies a disk space of about 13 Terabytes. These SGTs will be used to compute the Fréchet kernels for all the measurements from the 69 paths in the first step of an iterative full-wave 3D tomography.

CONCLUSIONS AND RECOMMENDATIONS

Significant progress has been made in developing and validating finite-frequency sensitivity kernels for 3D velocity and attenuation reference models. The finite-frequency head wave kernels will allow us to extend Pn/Sn tomography from presently 2D to 3D. The cross coupling between S-velocity perturbations and P waveforms provides a more accurate account of the forward problem. Together with the velocity models, the finite-frequency solutions of attenuation yield a self-consistent structure required by observed waveforms. We are applying the fully 3D kernels to synthetic tomography as well as real data in selected regions. In general, the scale of the study area to which we can apply the fully 3D finite-frequency tomography is linearly proportional to the available computational power. Finally, substantial efforts are needed to develop the method for large-scale 3D models and models with anisotropy.

REFERENCES

Aki, K., and P.G. Richards (2002). *Quantitative Seismology*, University Science Books.

Al-Lazki, A., D. Seber, E. Sandvol, N. Turkelli, R. Mohamad, and M. Barazangi (2003). Tomographic Pn velocity and anisotropy structure beneath the Anatolian plateau (eastern Turkey) and the surrounding regions, *Geophys. Res. Lett*., 30(24), doi:10.1029/2003GL017391.

Ben-Menahem, A. and S. J. Singh (1981). *Seismic Waves and Sources*, Springer-Verlag, New York.

Dahlen, F.A., S.-H. Hung, and G. Nolet (2000). Fréchet kernels for finite frequency traveltimes-I. Theory, *Geophys. J. Int.* 141: 157–174.

Gok, R., E. Sandvol, N. Turkelli, D. Seber, and M. Barazangi (2003). Sn attenuation in the Anatolian and Iranian plateau and surrounding regions, *Geophys. Res. Lett*. 30(24): 8042, doi:10.1029/2003GL018020.

Hearn, T.M., S. Wang, J.F. Ni, Z. Xu, Y. Yu, and X. Zhang (2004). Uppermost mantle velocities beneath China and surrounding regions, *J. Geophys. Res.* 109: doi:10.1029/2003JB002874.

Karato, S. (1993). Importance of anelasticity in the interpretation of seismic tomography, *Geophys. Res. Lett.* 20: 1623–1626.

Olsen, K.B. (1994). Simulation of three-dimensional wave propagation in the Salt Lake Basin, Ph.D. Thesis, University of Utah, Salt Lake City, Utah, 157p.

Ritzwoller, M.H., M.P. Barmin, A. Villasenor, A.L. Levshin, and E.R. Engdahl (2002). Pn and Sn tomography across Eurasia to improve regional seismic event locations, *Tectonophysics* 358: 39–55.

Sandvol, E., N. Turkelli, E. Zor, R. Gok, T. Bekler, C. Gurbuz, D. Seber, and M. Barazangi (2003a). Shear wave splitting in a young continent-continent collision: An example from Eastern Turkey, *Geophys. Res. Lett*. 30: (24), 8041, doi:10.1029/2003GL017390.

Sandvol, E., N. Turkelli, and M. Barazangi (2003b). The eastern Turkey seismic experiment: The study of a young continent-continent collision, *Geophys. Res. Lett*. 30: (24), 8038, doi:10.1029/2003GL018912.

Turkelli, N., E. Sandvol, E. Zor, R. Gok, T. Bekler, A. Al-Lazki, H. Karabulut, S. Kuleli, T. Eken, C. Gurbuz, S. Bayraktutan, D. Seber, and M. Barazangi (2003). Seismogenic zones in Eastern Turkey, *Geophys. Res. Lett*. 30: 8039, doi:10.1029/2003GL018023.

Walter, W.R., M.E. Pasayanos, J. Bhattacharyya, and J. O'Boyle (2000). MENA 1.1 – An updated Geophysical regionalization of the Middle East and North Africa, UCRL-ID-138079, Lawrence Livermore National Laboratory Report.

Zhang, Z., Y. Shen, and L. Zhao (2007). Finite-frequency sensitivity kernels for head waves, *Geophys. J. Int*, accepted for publication.

Zhao, L. and P. Chen (2006). A full-wave approach to elastic and Q tomography, *EOS Trans. AGU* 87: (52), Fall Meet. Suppl., Abstract S53C-04.

Zhao, L., T.H. Jordan, and C.H. Chapman (2000). Three-dimensional Fréchet differential kernels for seismic delay times, *Geophys, J. Int.* 141,:558–576.

Zhao, L., P. Chen, and T.H. Jordan (2006). Strain Green tensor, reciprocity, and their applications to seismic source and structure studies, *Bull. Seism. Soc. Am*. 96: 1753–1763, doi:10.1785/0120050253.

Zhao, L., T.H. Jordan, K.B. Olsen, and P. Chen (2005). Fréchet kernels for imaging regional earth structure based on three-dimensional reference models, *Bull. Seism. Soc. Am.* 95: 2066–2080.

Zor, E., E. Sandvol, C. Gurbuz, N. Turkelli, D. Seber, and M. Barazangi (2003). The crustal structure of the East Anatolian plateau (Turkey) from receiver functions, *Geophys. Res. Lett*. 30: 8044, doi:10.1029/2003GL018192.

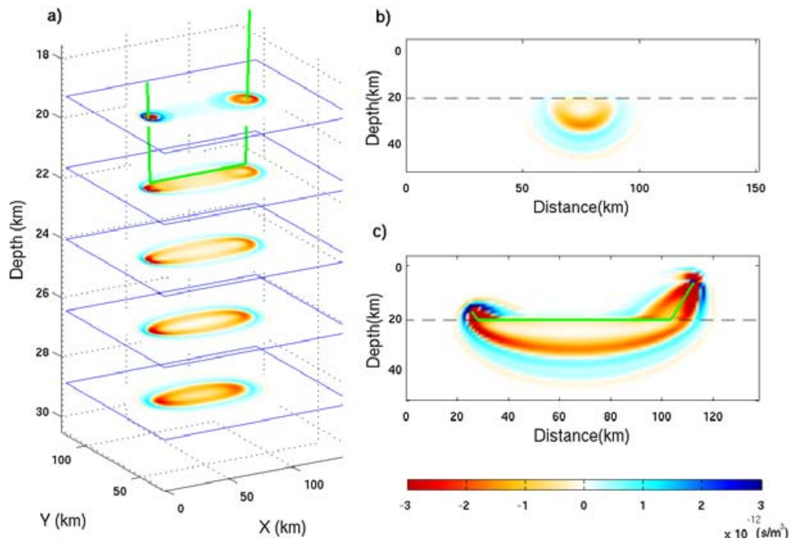

Figure 1. (a) The travel-time sensitivity kernels for the head wave recorded on the vertical component on the horizontal planes at depths below (21.6 km, 24 km, 26.4 km, 28.8 km) and above (19.2 km) the interface that separates the low and high velocity layers. The interface, source and receiver are at 21.4, 18, and 6.4 km depth, respectively. The P, S velocities and the density of the first layer are 5207 m/s, 3189 m/s and 2950 kg/m^3 respectively; those of the half space 9058 m/s, 5307 m/s and 3992 kg/m^3. The finite-difference model for simulating wave propagation has a regular grid of 280 x 301 x 126 in the source-receiver, transverse, and vertical directions, with a grid spacing of 400 m. The source time function has a dominant period of about 1.2 second. The green line marks the head wave ray path. The source is located on the left side of this figure. The negative (red colors) and positive (blue colors) values are so defined that a low-velocity anomaly located in the region of the negative kernels results in a travel-time delay and the same velocity perturbation in the region of positive kernels leads to an earlier head wave arrival. (b) The travel-time sensitivity kernel for the head wave on a vertical profile half way between the source and receiver and perpendicular to the ray path. The dashed line is the layer interface. (c) The travel-time sensitivity kernels for the head wave on the vertical profile containing the source and receiver.

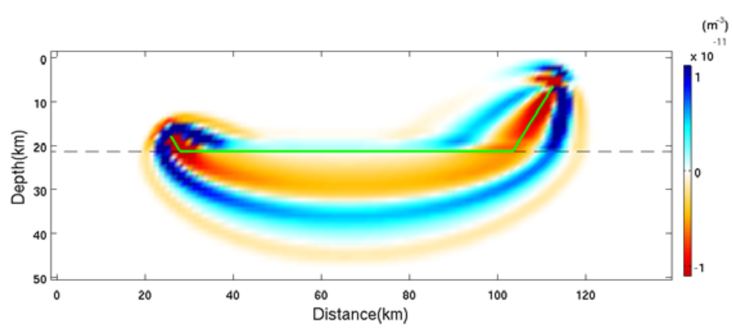

Figure 2. Amplitude sensitivity kernels for the vertical component of the head wave on the vertical profile containing the source and receiver. The dashed line indicates the layer interface and the green line highlights the ray path. The negative (red colors) and positive (blue colors) values are so defined that a low-velocity anomaly in the red region causes an amplitude increase and the same velocity anomaly in the blue region leads to a reduction in the amplitude of the head wave.

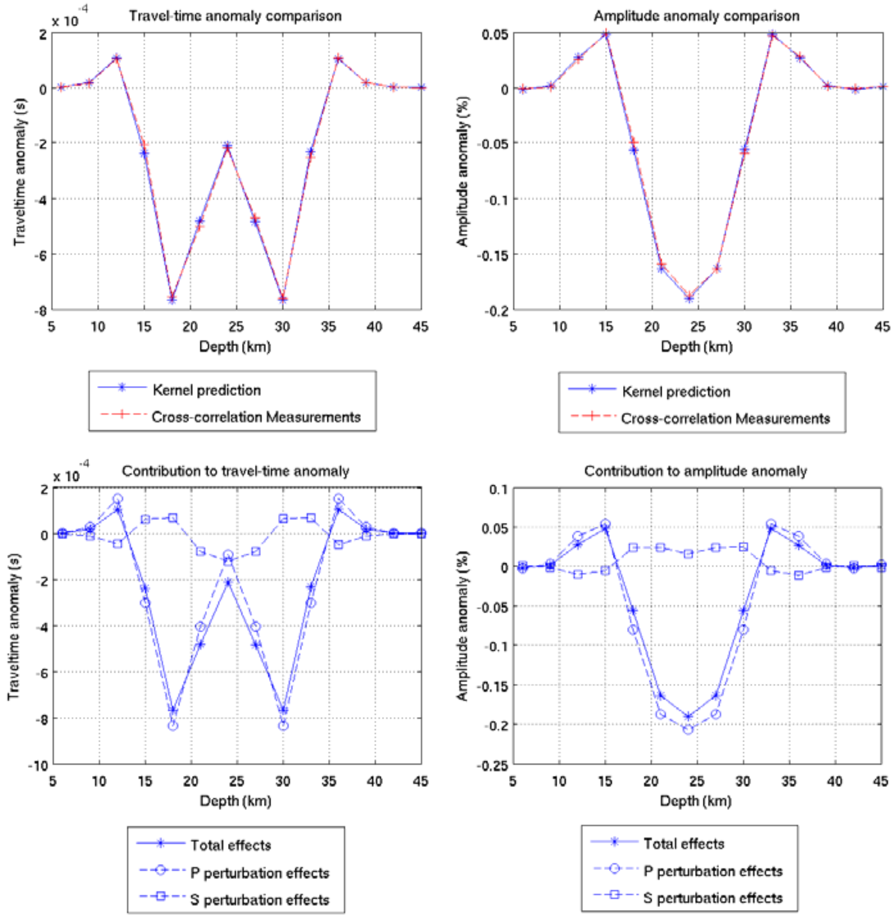

Figure 3. (upper panels) A comparison of the kernel predictions (stars) and waveform cross-correlation measurements (crosses) of travel-time and amplitude anomalies of a P wave from an explosive source. A cylindrical-shaped velocity perturbation of 3% Vp and Vs with a height of 6 km and the radius of 3 km is placed along a vertical profile in the middle between the source and receiver. Each symbol represents one simulation with the perturbation centered at a particular depth. See the text for additional information about the numerical experiments. Both travel-time and amplitude predictions match the direct waveform cross-correlation measurements well. (lower panels) The contributions of the travel-time and amplitude anomalies from the P-velocity perturbation (circles) and the S-velocity perturbation (crosses). Neglecting the S-velocity contribution, as in common practice, causes significant misfits.

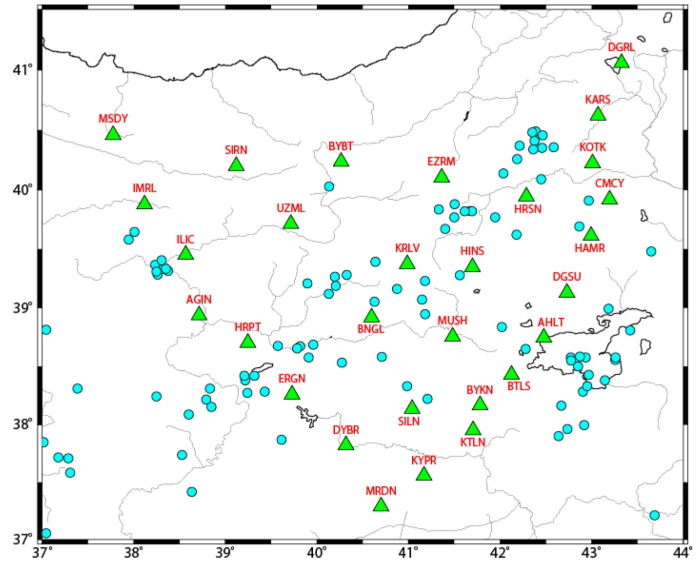

Figure 4. Data collection from the Eastern Turkey Seismic Experiment (ETSE). Triangles indicate the locations of the 29 ETSE stations, and circles show the epicenters of the 124 events located by ETSE (Turkelli et al. 2003).

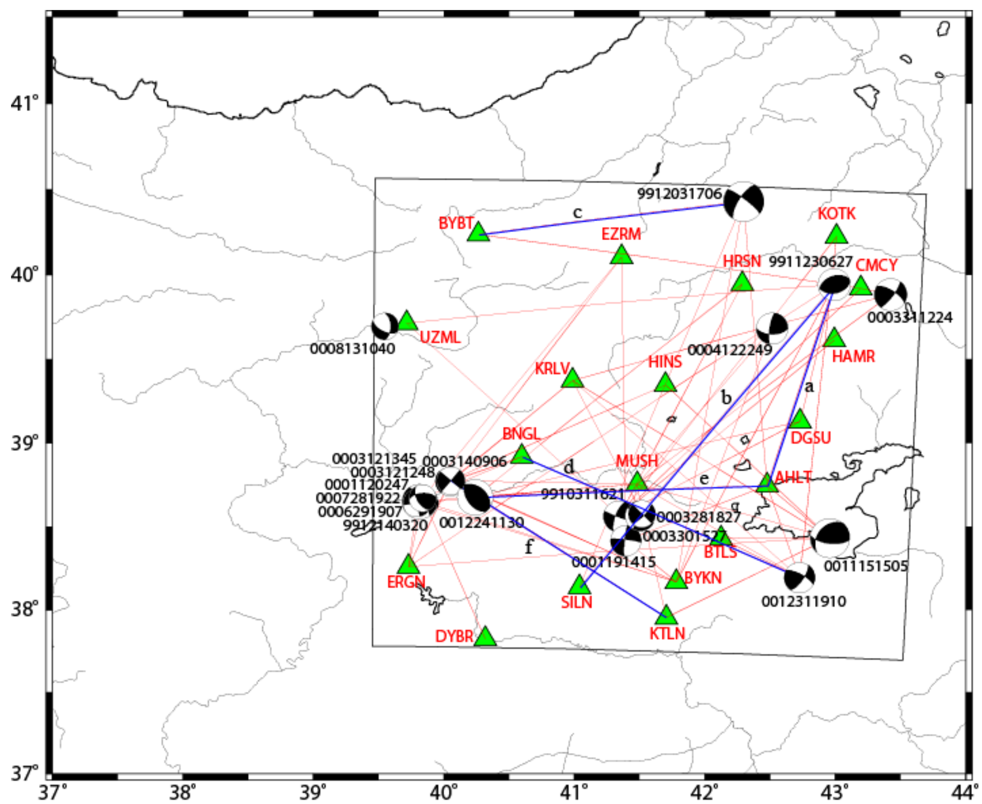

Figure 5. Full-wave tomography using the ETSE dataset. Boxed region shows the current study area. Triangles and beachballs show the locations of the 19 stations and 24 events with focal mechanism solutions (Turkelli et al. 2003) used so far in our tomography study, resulting in 69 source-receiver paths (red lines). Blue lines indicate the source-receiver paths whose frequency-dependent phase and amplitude anomaly measurements are shown in Figure 6.

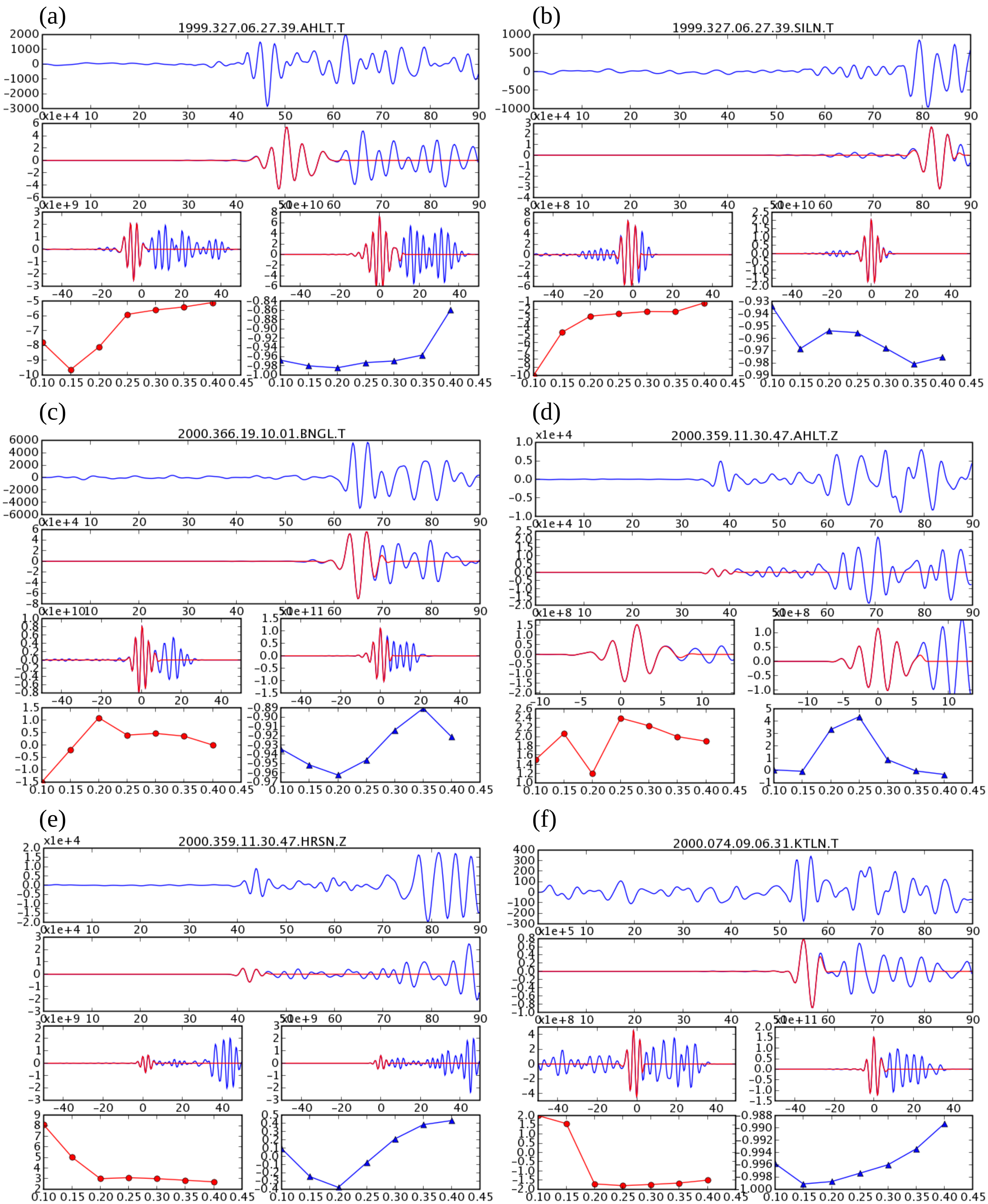

Figure 6. Frequency-dependent phase and amplitude anomaly measurements obtained from the paths (a)-(f) shown in Figure 5. In each panel, the top two traces are recorded and synthetic seismograms (Z for vertical and T for transverse) with the red line showing the synthetic in the time window of interest. In the third row are the cross-correlation (left) and auto-correlation (right) defined in eqs.(1) and (4), respectively. The bottom row shows the phase (left) and amplitude (right) anomalies at seven frequencies between 0.1 Hz and 0.4 Hz.